# Stress on the Mediterranean Outflow Plume: Part I. Velocity and Water Property Measurements

GREGORY C. JOHNSON

*Applied Physics Laboratory, University of Washington, Seattle, Washington*

THOMAS B. SANFORD

*Applied Physics Laboratory and School of Oceanography, University of Washington, Seattle, Washington*

MOLLY O'NEIL BARINGER

*MIT–WHOI Joint Program, Woods Hole Oceanographic Institution, Woods Hole, Massachusetts*

(Manuscript received 4 March 1993, in final form 11 January 1994)

ABSTRACT

In September 1988 six sections were occupied across the Mediterranean outflow plume in the Gulf of Cadiz within 100 km of the Strait of Gibraltar. Vertical profiles of temperature and salinity were collected at CTD stations. Velocity and temperature profiles were collected with expendable current profilers at a subset of these stations. At the channel base, the plume undergoes geostrophic adjustment and turns northwest to flow along the continental slope. There it decelerates and spreads gradually down the slope as friction slows the current and allows it to cross isobaths. Within the plume, downstream velocity and density increase rapidly in the interfacial layer with depth to the velocity maximum, or nose, 5–150 m above the bottom. Below the nose, in the bottom layer, downstream velocity decreases rapidly toward the bottom, but the stratification is weak. Ekman-like veering occurs in the interfacial layer. Local bottom stresses on the plume are estimated by fitting the near-bottom velocity profiles to a log-layer model. These stresses are compared with bulk estimates of total stresses from momentum budget residuals and of interfacial stresses from combining the mean vertical shear with bulk turbulent dissipation estimates. The downstream pattern of the sum of the local bottom stresses and the bulk interfacial stresses agrees well in magnitude and distribution with that of the bulk total stresses. The largest stresses reach a mean of 5 Pa where the plume is flowing rapidly westward down a channel after exiting the strait, thinning, and accelerating. These stresses are an order of magnitude larger than mean wind stress values over the ocean gyres and exceed most bottom stress estimates in other regions.

## 1. Introduction

Velocity and water property data are used to gain insight into the dynamics of the Mediterranean outflow plume and estimate bottom and interfacial stresses acting on the plume. First, the roles of stress and entrainment in maintaining the horizontal and vertical water mass and velocity structure within the plume are discussed. Direct measurements of velocity within the more ageostrophic regions close to the strait allow accurate estimates of transports and entrainment rates there. Bottom stresses are calculated by fitting the velocity data to a log-layer model. Bulk interfacial stresses on the plume are estimated using residuals of mass and volume transports through sections made across the plume. The expendable current profiler (XCP) and CTD data are used to construct a bulk momentum budget and infer the total stresses on the plume from downstream changes in the Bernoulli potential (Baringer 1993). The magnitude and spatial distribution of these estimates of total stress agree with those from the sum of bottom and interfacial stress values.

The Mediterranean Sea is a basin where dry, continental winds cool and evaporate water at the surface, creating salty, dense water. This water is so dense that an undiluted parcel of it would sink directly to the bottom in the North Atlantic Ocean. The density difference between light, fresh North Atlantic Central Water (NACW) and dense, salty, Mediterranean Water (MW) drives an exchange of water at the Strait of Gibraltar. The MW flows westward toward the Atlantic just above the bottom of the strait. The NACW flows eastward near the surface. This exchange is often discussed in the context of hydraulic control theory (Armi and Farmer 1988). Recent mean volume transport estimates for the outflow are about $0.8 \times 10^6$ m$^3$ s$^{-1}$

*Corresponding author address:* Dr. Gregory C. Johnson, NOAA/Pacific Marine Environmental Laboratory, 7600 Sand Point Way N.E. Bldg. 3, Seattle, WA 98115-0070.

(Bryden and Kinder 1991), half the result of tidal rectification within the strait (Bryden et al. 1989). There is also variability of up to $1.0 \times 10^6$ m$^3$ s$^{-1}$ in net volume transport forced by synoptic weather patterns (Candela et al. 1989).

After the MW exits the Strait of Gibraltar, it cascades rapidly westward down a channel into the Gulf of Cadiz. It then turns and flows nearly parallel to the bathymetry along the gulf's northern side under the influence of rotation. It slowly spreads down the continental slope as it flows toward the Atlantic. Along this path, the MW mixes considerably with the surrounding NACW so that when the current passes Cape St. Vincent it is at an equilibrium depth near 1200 m (Price et al. 1993). This mixing is evident in the spatial distribution of potential temperature–salinity ($\theta$–$S$) characteristics within the plume. In addition, it is possible to discern upper and lower outflow branches with distinct water mass properties (Ambar and Howe 1979). Recently, hydrographic data have been used to make estimates of the outflow transport. Application of inverse methods to several sections made across the gulf suggest a pattern of entrainment and mixing (Ochoa and Bray 1991). The complex bathymetry in the gulf (Heezen and Johnson 1969), coupled with the bottom-trapped nature of the plume and strong ageostrophic flow near the strait, makes estimates of these processes with hydrographic data alone uncertain.

Upon exiting the Gulf of Cadiz some MW turns to flow northward at middepth along the European continental slope, eventually reaching the surface in the Norwegian–Greenland Sea. The high salinity of the MW contributes significantly to the density of the component of North Atlantic Deep Water formed there. Thus the MW plays a significant role in the global thermohaline circulation (Reid 1979). The remaining MW spreads to form the salt tongue that extends westward at middepth across the North Atlantic (Worthington 1976). Some of the outflow goes into the generation of long-lived submesoscale coherent vortices of MW, or meddies (McDowell and Rossby 1978; Armi et al. 1989). Through self-propagation and advection, these meddies move to the southwest (Killworth 1983) and decay (Hebert et al. 1990).

Smith (1975) formulated a streamtube model for a gravity current moving over a sloping bottom in the presence of rotation to gain insight into the dynamics of the Mediterranean outflow plume where it is moving rapidly and entraining NACW. He tuned the magnitudes of friction and entrainment to match the observed downstream evolution of density anomaly and velocity within the plume. More recently, a model of the outflow was con-

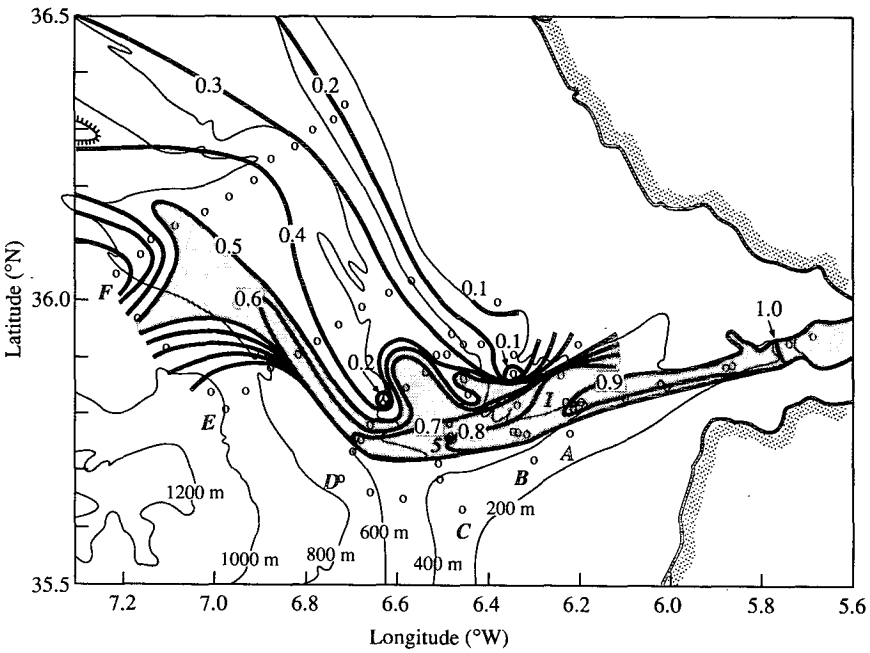


FIG. 1. Location of CTD stations (open circles) with contours of maximum Mediterranean Water fraction at 0.1 intervals (thick lines; see section 3 and Fig. 3 for a discussion of MW fraction) showing the Mediterranean outflow plume. The plume spreads and dilutes as it flows to the northwest, sliding slowly down the continental shelf. MW fraction above 0.5 is stippled and contour lines merge in regions of sharp gradients near the plume edges. Sections A–F and sites 1 and 5 are labeled to their south and west, respectively. Bathymetry from Heezen and Johnson (1969) is contoured at 200-m intervals (thin lines).

structed using a quadratic drag law (with a fairly large drag coefficient of $3 \times 10^{-3}$) and a Froude number–dependent entrainment (Baringer and Price 1990). It was necessary to use a realistic (if smoothed) bathymetry for reasonable agreement with observations since the plume speed is strongly dependent on bottom slope.

Here we show that bottom and interfacial stresses are large and significant in shaping the vertical velocity and water mass structure of the plume. In a companion paper Johnson et al. (1994, hereinafter JLS) combine measurements of small-scale vertical shear from expendable dissipation profiler (XDP) data with the velocity data to make independent estimates of bottom and interfacial stress within the plume. These estimates are roughly a factor of three smaller than those presented here. This discrepancy is discussed at length in JLS.

## 2. Data

The Gulf of Cadiz Experiment was conducted in September 1988 (Kennelly et al. 1989a). A subset of 72 of the 99 CTD stations occupied during the week-long outflow component of the experiment (Kennelly et al. 1989b) is used to describe the water mass structure of the outflow plume (Fig. 1) in section 3. Six synoptic sections were made across the outflow plume. In addition, there were duplicate occupations at nine sites, with multiple occupations at two of these sites. The CTD was generally lowered to within 10 m of the bottom and the data were averaged in 2-m bins.

Where the CTD data indicated the presence of the plume, an XCP (Sanford et al. 1982) was usually dropped just after the CTD station was completed (Kennelly et al. 1989c). The XCPs yield vertical profiles of velocity and temperature with values every 0.28 m to within $0.56 \pm 0.14$ m of the bottom. The fall rate has been corrected by comparing bandpassed structure of the XCP temperature profiles with those from CTD stations occupied just prior to the XCP drops (Prater 1991). Of the 64 XCP drops during the outflow component of the experiment, 4 malfunctioned, 3 were outside the plume, and 3 were east of the Camarinal Sill, leaving 54 XCP drops within the outflow plume (Fig. 2). The reference velocity is unknown, so the vertical mean of the horizontal velocity has been removed from each profile. This adjustment forces a balance between the outflow and the inflow above. A prior study suggests that the inflow may indeed be directly above the outflow (Ochoa and Bray 1991). Since the outflow is relatively thin and fast, and the inflow above is thick and slow, small adjustments to the velocities will not affect the outflow transport as much as that of the inflow.

## 3. The plume

CTD data similar to those from the Gulf of Cadiz expedition have been collected in other surveys (Ambar and Howe 1979; Ochoa and Bray 1991). In contrast, the vertical resolution of the velocity profiles from the XCPs is exceptional. Vertical profiles of density and velocity from the CTD and XCP data combine to reveal the rich vertical structure of the plume. This structure varies spatially in the survey region. Data from the repeatedly occupied site 5 at the core of the plume in section C (Fig. 1) demonstrate the lack of temporal variability throughout the survey. Site 5 was occupied six times during the survey. Four of the XCP drops (2529, 2544, 2556, and 2580) at this site were nearly at the same location (within a circle of 800-m radius). All four reached the bottom within 2 m of 497 m. They were made at 0, 4.08, 5.51, and 13.20 cycles of the 12.4-h period $M_2$ tide with phase relative to XCP 2529. CTD casts were made for three of these four XCP drops. All the profiles show remarkably similar velocity and density structure within the plume, hence negligible tidal influence. The plume appears steady during the survey.

### *a. Water mass structure of the plume*

The temperature–salinity curves at site 5 show several features common throughout the survey region (Fig. 3). The ambient NACW in the gulf is relatively fresh, less than 36 psu near the plume depth. A fifth-order polynomial curve (the solid line at the left of the plot) has been fit to the NACW using data from CTD casts in the outer region of the gulf in deeper water where the NACW $T$–$S$ curve extends the full length of the line. Pure MW ($T = 12.92°C$; $S = 38.45$ psu) is represented by the asterisk at the far right of the plot. The plume $T$–$S$ curves within the survey region are nearly linear, stretching from one end member at the NACW toward the MW. This near linearity suggests that vigorous mixing is taking place within the plume between the NACW above and the MW below. The slight upward bowing of the curves (Fig. 3) is the result of the plume descending through and mixing with NACW of varying $T$–$S$ characteristics. As the plume descends, the temperature of the ambient NACW end member changes from warm to cold, and the upward bowing of the $T$–$S$ curves is the memory of this change. This feature occurs because where the plume is shallow, the water within the plume sees an NACW end member that is warmer than the MW. Downstream, where the plume is deeper, the NACW end member is colder than the MW. The density anomaly of the NACW that mixes with the MW is $\sigma_t = 26.8$–$27.4$ kg m$^{-3}$, and pure MW has $\sigma_t = 29.1$ kg m$^{-3}$. The plume is primarily salinity stratified.

The MW fraction at any given point can be determined by assuming that data in the plume lie on a straight mixing line in $T$–$S$ space between the MW end member and an NACW end member (Fig. 3; McDougall 1990; Bormans and Turner 1990). A line can

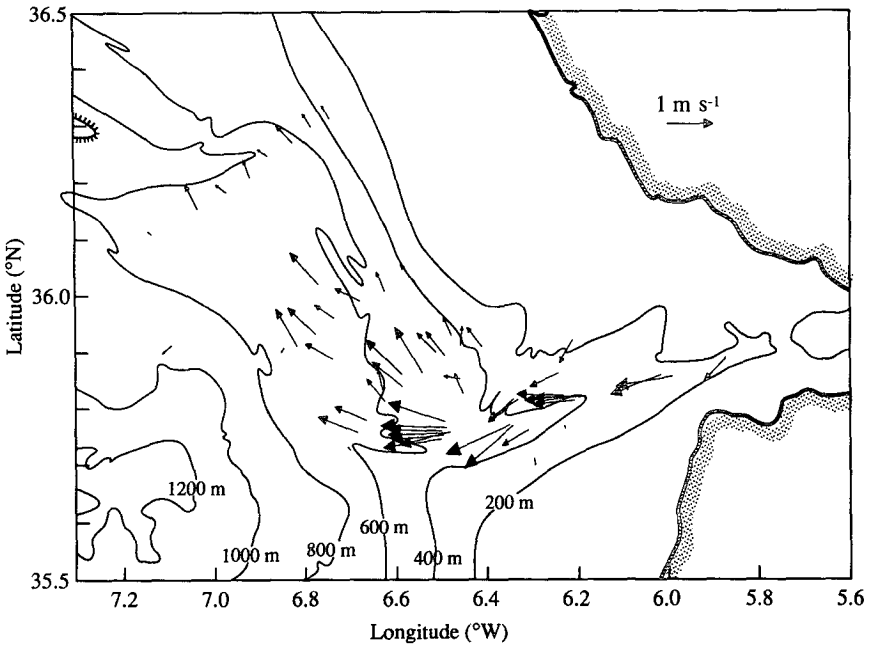


FIG. 2. Maximum plume velocities, or nose velocities, from 54 XCPs dropped within the outflow plume. The arrow tails mark the drop locations. The plume accelerates flowing west down the channel between sections A and C (see Fig. 1), then turns northwest, nearly following isobaths, and slows, gradually sliding down the continental shelf. Bathymetry from Heezen and Johnson (1969) is contoured at 200-m intervals.

be drawn from the MW end member through the data point in question. The NACW end member is defined by the intersection of this line and the NACW curve. The MW fraction is the ratio of the line length from the NACW end member to the data point and the line length from the NACW end member to the MW end member. This MW fraction gives a quantitative measure of the mixing of the plume with the NACW. Pure NACW has an MW fraction of zero, and pure MW has a value of one. The MW fraction is related in a nearly linear fashion to salinity and density (Fig. 3). The MW fraction is highest at the bottom in this region and decreases to the northwest after the plume leaves the strait (Fig. 1).

### *b. Vertical structure of the plume*

The vertical water mass structure of the plume is linked to the vertical structure of horizontal velocity. As mentioned above, the vertical mean of horizontal velocity is subtracted from each profile. The velocity is then rotated into plume coordinates such that the velocity difference between the depths of the temperature minimum (near the top of the plume) and speed maximum (also referred to as the plume nose) defines the direction of the downstream axis for each profile. The cross-stream axis is positive 90° to the right, so cross-stream velocity is the $u$ component and downstream velocity is the $v$ component of a right-handed coordinate system.

The plume is composed of two layers, an interfacial layer and a bottom layer, that meet at the plume nose, where the downstream velocity is a maximum. At site 5, the MW fraction increases rapidly and nearly linearly with depth from 0 at about 350 m to near 0.8 around 430 m, and then much more slowly to around 0.85 about 10 m off the bottom at 490 m (Fig. 4). The downstream velocity starts near $-0.3$ m s$^{-1}$ at 350 m and increases to a maximum of 1.2 m s$^{-1}$ near 430 m, a change of 1.5 m s$^{-1}$ over about 80 m. Below the maximum, the downstream velocity decreases rapidly, approaching zero at the bottom (near 500 m). The only significant cross-stream velocity occurs at the interfacial layer, where peak values reach 0.3 m s$^{-1}$. Hence there is an 80-m thick, highly stratified, highly sheared interfacial layer, where mixing between the MW and the NACW keeps gradients nearly linear, and a slightly stratified but strongly sheared bottom layer of similar thickness where mixing serves to homogenize the MW. The plume nose is a minimum in shear. This minimum may impede vertical mixing. Supporting this assertion, most of the vertical profiles of turbulent dissipation in the plume have a local minimum near the nose (JLS). The nose may insulate the two layers, but there must be some mixing across it because the MW fraction in the bottom layer steadily decreases down-

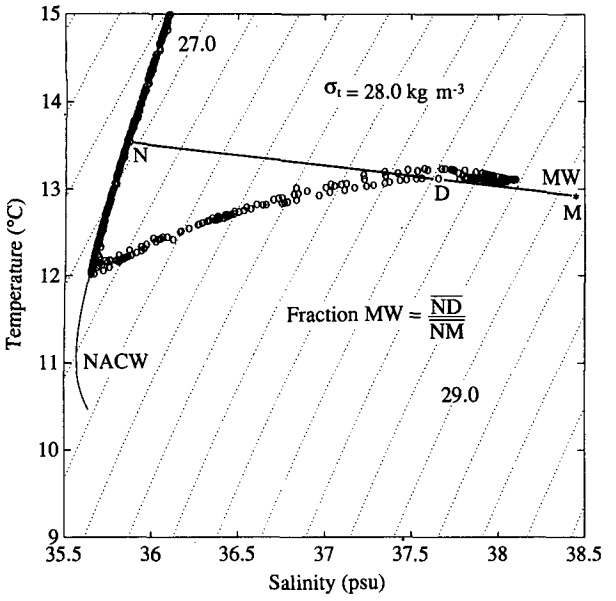


FIG. 3. Temperature–salinity ($T$–$S$) data at 2-m intervals (open circles) from site 5 (Fig. 1), CTD stations 55, 75, and 91. The North Atlantic Central Water (NACW) $T$–$S$ curve is a fifth-order polynomial (solid line) that is obtained from a fit to $T$–$S$ data west of site 5, where the NACW extends over the full temperature range of the curve. The Mediterranean Water end member (asterisk) is a point ($T$ = 12.92°C; $S$ = 38.45 psu). Isopycnals ($\sigma_t$) are contoured at 0.2 kg m$^{-3}$ intervals (dotted lines). The MW fraction at D is the ratio of $\overline{ND}$ to $\overline{NM}$ (McDougall 1990; Bormans and Turner 1990). The nearly linear $T$–$S$ curves of the plume suggest vigorous mixing.

stream (Fig. 1). While there is little evidence of intrusion in the $T$–$S$ curves east of section $F$, lateral mixing may also play some role in the plume evolution.

The cross-stream velocity structure is unexpected. Because there are strong stresses in the bottom layer, there should be veering as in a planetary boundary layer (Holton 1979), clockwise with increasing height above the bottom. Rotation of the velocity vector is in the expected sense, but not in the bottom layer, where the shear is nearly unidirectional and velocity is in the downstream direction. The cross-stream velocity is significantly positive only in the interfacial layer, indicating a veering there (Fig. 4), where the stratification is largest. One possible explanation for this structure is that the scale height of the bottom Ekman layer is larger than the bottom layer itself, so there can be little veering there (Gammelsrød 1975). A crude scale analysis using the friction velocities from the log-layer analysis below, along with the nose velocity and its height above the bottom, gives Ekman heights that nearly always exceed the bottom-layer thickness. On average, the Ekman height is more than twice the bottom-layer thickness. As a result, the entire bottom layer moves slightly to the left of the flow within the interfacial layer. The net effect is that more of the denser bottom layer flows across isobaths into deeper water than the lighter interfacial layer. The veering causes the plume to spread laterally as it flows along the continental slope in the Gulf of Cadiz (Figs. 1 and 2).

### c. *Horizontal structure of the plume*

The maximum MW fraction is always found at the bottom of CTD casts in the survey region (Fig. 1), where the plume is bottom trapped and salinity stratified (Fig. 3). Pure MW is found near the bottom east of the Camarinal Sill at 5°50′W. The plume core (defined as the maximum MW fraction at a section) mixes with NACW as it moves west and flows down a channel to section C. Near section C, the plume core follows the topography to the northwest and runs nearly parallel to the isobaths to section F, with a slight downslope tendency. The plume core deepens with increasing distance from the sill. By section F, the maximum MW fraction is diluted to just above 0.5 (Fig. 5).

The nose (maximum downstream) velocity starts near 1.0 m s$^{-1}$ at section A, accelerates to 1.3 m s$^{-1}$ by section C, then slows to a peak of 0.6 m s$^{-1}$ at section F (Fig. 2). The flow is westward down the channel from section A to section C. At the base of the channel, the flow turns to run nearly parallel with the isobaths, with only a small downslope component.

Volume and mass transport of the plume, calculated perpendicular to each of the six sections, are used below

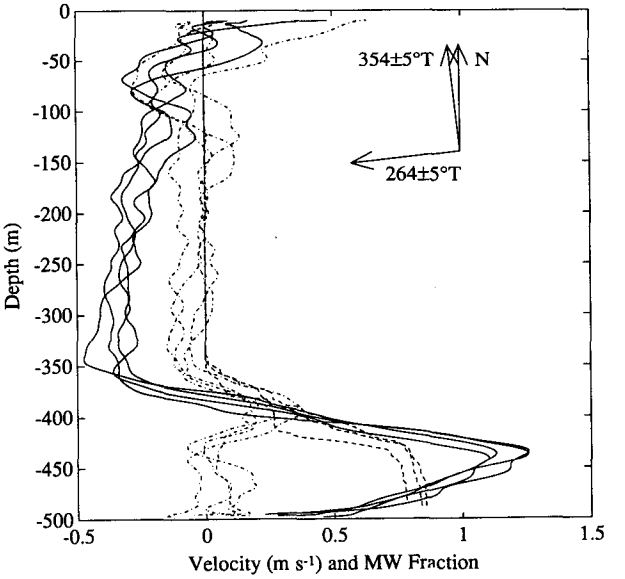


FIG. 4. Downstream (solid line; 264 ± 5°T) and cross-stream (dot-dashed line; 354 ± 5°T) velocity from site 5 XCP drops 2529, 2544, 2556, and 2580. Mediterranean Water fraction (Fig. 3) from the CTD data is also plotted (dashed line; see Fig. 3). Downstream velocity and MW fraction increase rapidly from 350 m to 430 m in the interfacial layer. In the bottom layer, downstream velocity decreases rapidly but MW fraction increases slowly. The positive cross-stream velocity in the interfacial layer veers in the sense of a planetary boundary layer there.

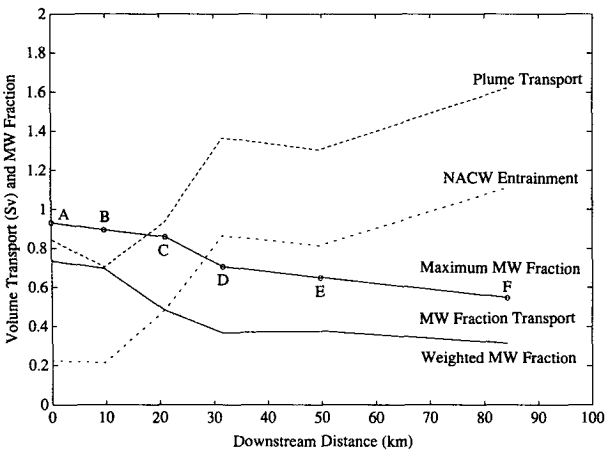


FIG. 5. Volume transport and MW fraction against downstream distance. The MW fraction transport (dotted line) is nearly constant. The plume transport (dashed line) doubles owing to NACW entrainment (dot–dashed line). The increase is largest between sections B and D, where transport-weighted MW fraction (solid line) decreases most. Maximum MW fraction (solid line with open circles) decreases more linearly.

to make bulk estimates of the turbulent buoyancy flux into the plume in section 4b. For each XCP velocity profile within a section, the velocity component perpendicular to the section is found. The top of the plume is determined by the zero crossing of this component of the velocity, and then this quantity is integrated, profile by profile, over the cross-sectional area of the plume for each section to determine the volume transport there (plume transport; Fig. 5). The plume transport doubles from 0.8 to 1.6 Sv (Sv $\equiv 10^6$ m$^3$ s$^{-1}$) from section A to section F.

The net transport of pure MW within the plume (MW fraction transport; Fig. 5) can be calculated by multiplying the velocity component perpendicular to the section by the MW fraction before integrating. Since the NACW curve is nearly linear, the MW fraction transport should be nearly conservative; it turns out to be 0.51 $\pm$ 0.05 Sv (std dev) for the six sections. Using the deviation of each section from the average MW fraction transport, the weighted MW fraction at each section, and the cross-sectional area of the plume at each section, the differences of velocity components perpendicular to the sections and MW fraction transport-conserving velocities are found to have a standard deviation of 0.05 m s$^{-1}$. This calculation suggests that the subtraction of the vertical mean of the horizontal velocity from each profile gives a good approximation of the actual velocities within the plume.

The difference of the plume transport and MW fraction transport gives NACW entrainment (Fig. 5). Since this quantity is a difference, it is less subject to the sampling problems, from either the quasi-synoptic nature of the survey or the limited number of profiles in each section, that probably cause the decrease in plume transport from section A to section B and the small variability in MW fraction transport among the sections. The NACW entrainment increases most rapidly between sections B and D. Another way of evaluating entrainment is to calculate the (transport) weighted MW fraction by dividing the MW fraction transport by the plume transport (Fig. 5). Again, there is a large change between sections B and D, whereas the maximum MW fraction (Figs. 1 and 5) decreases more linearly with downstream distance.

## 4. Stress within the plume

Two methods are used to infer the stress on the plume. The first method uses the law of the wall to estimate local friction velocities, $u_*$, at the bottom of the plume from XCP velocity data. These friction velocities are then converted to bottom stress values. Local values are averaged to obtain a mean bottom stress for each section. The second method uses differences of volume and mass transports through the sections to make bulk estimates of the turbulent buoyancy flux through the top of the interfacial layer. The buoyancy flux is assumed to be proportional to the dissipation. Bulk stresses in the interfacial layer are determined by dividing the sum of the estimated turbulent buoyancy flux and dissipation by the mean shear in the interfacial layer. These bulk estimates give mean values of interfacial stress between sections. We show below that these section averages of bottom stress, combined with bulk values of interfacial stress, have a pattern consistent with that derived from the residuals of a downstream momentum budget (Baringer 1993).

### *a. Using XCP velocity profiles to estimate bottom stress*

The "profile method" is used to estimate the magnitude, direction, and spatial distribution of the bottom stress within the plume (Jones 1989; Johnson and Sanford 1992). The velocity data near the bottom are fitted to a turbulent boundary layer modeled with the law of the wall, which predicts a mean velocity profile of the form

$$U(z) = \frac{u_*}{\kappa} \ln\left(\frac{z}{z_0}\right), \qquad (1)$$

within the constant stress layer. Here, $U(z)$ is the mean velocity, $u_*$ the friction velocity, $\kappa = 0.4$ von Kármán's constant, and $z_0$ the roughness length. The height above the bottom is given by $z$. Owing to the shape of the velocity profile, this portion of the bottom boundary layer is known as the log layer. Since the absolute velocities are unknown, roughness lengths are not estimated. A friction velocity is found for each drop using the slope of a least-squares fit of velocity to the log of

the height above the bottom (Fig. 6). The stress is shown to oppose the mean direction of the plume.

The magnitude and direction of the friction velocity depend on the height over which the fit is made. We adopt a procedure such that the criterion for choosing the height of the fit is uniform for all the profiles. First, the top of the constant-temperature layer is identified. For these purposes a deviation of about 0.02°C (slightly above the XCP quantization level) from the near-bottom values serves as the top of the constant temperature layer. Then, a series of fits is made for each profile, starting with the bottom two points, then the bottom three, and so on through the fit using all the points in the constant temperature layer. The magnitudes and directions of the resulting friction velocities, along with the correlation coefficients of the fits, are then plotted against the maximum height above the bottom of each fit. For each profile the fit chosen has the fewest points while maintaining a high correlation coefficient and a magnitude and direction stable with respect to fits extending higher off the bottom. Making the fits over a region as close to the bottom as possible assures that the friction velocity estimates are within the log layer.

There are 54 XCP drops within the densely sampled area of the plume. One drop yielded very noisy data that do not fit (1) well. Two drops had no region of constant temperature and thus were in a stratified region ill suited to modeling with (1). From the top of the plume to the nose, or velocity maximum, most of the remaining drops show a monotonic increase in downstream velocity. Four of these drops show a secondary maximum in velocity less than 10 m from the bottom. This double nose may be a signature of a local acceleration near topographic features, where the application of a 1D balance, such as (1), would not be appropriate. All seven of these drops are excluded from the estimation of friction velocities; the remaining 47 profiles are used.

The height of the log-layer fits range from 4 to 23 m above the bottom. The mean thickness of the log layer is 8 m and the median 7 m, with a standard deviation of 4 m. The regions of constant stress within the plume derived from XDP dissipation measurements are of very similar thickness (JLS). The log-layer heights used here are thus consistent with those estimated from the dissipation estimates.

The ratio of the squares of the friction and free-stream velocities is called a drag coefficient. A drag coefficient is usually calculated using a velocity at a fixed height above the bottom, unlike those of the plume nose. In addition, the nose velocities are less than the hypothetical free-stream velocity that might set a drag coefficient, because the nose is formed by the intersection of turbulent bottom and interfacial layers (JLS). With these caveats in mind, the ratio of the squares of the friction and nose velocities is 2.5 ($\pm 0.7$) $\times 10^{-3}$, (Fig. 7). The uncertainties are twice the standard error of the mean (95%). While this ratio is not a proper drag coefficient, it is similar to that used recently in a model of the plume (Baringer and Price 1990). There is no obvious variation of the ratio with the strength of the nose velocity. The ratio is used to estimate standard errors of the means for section averages of bottom stress.

The stress in the log layer opposes the nose velocity direction as expected (Fig. 8). Unexpectedly with re-

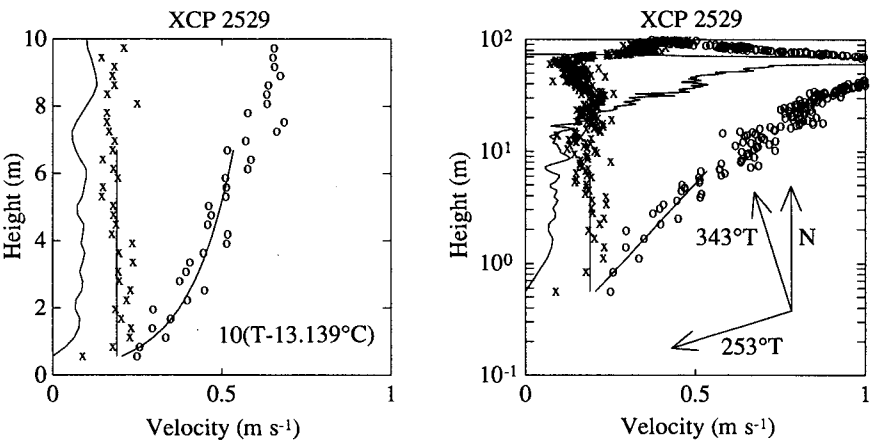


FIG. 6. Typical log-layer fit of a velocity profile, XCP 2529, at site 5. The left panel shows the bottom 10 m on a linear scale, the right panel the bottom 100 m on a logarithmic scale. Velocity data (open circles and crosses) are fitted to a line against log of height above the bottom and rotated such that all the shear is in one component of the fit, the stress direction (253°T). The fit slope is proportional to friction velocity. The height of the fit is chosen within the constant temperature layer, as close to the bottom as possible while maintaining a stable magnitude and direction of stress. Temperature (solid line) is relative to the bottom value with a range of 0.1°C full scale (13.139°–13.239°C).

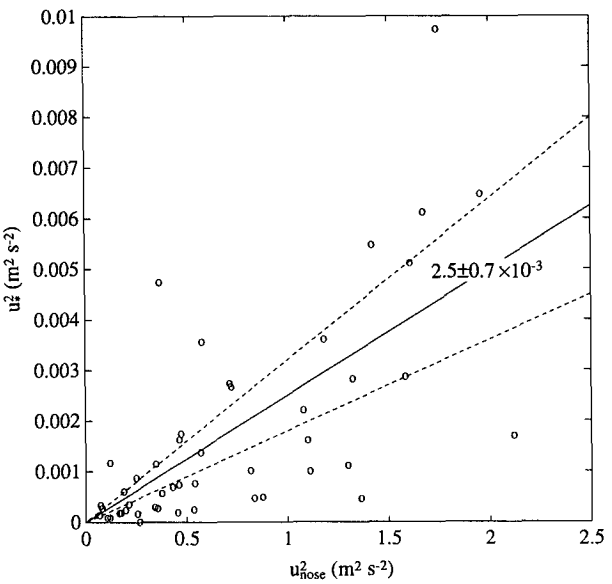


FIG. 7. Friction velocity squared against nose velocity squared. The ratio is $2.5(\pm 0.7) \times 10^{-3}$ (two standard errors of the mean, the 95% confidence level of the mean). Nose velocities vary in height above the bottom and are not free-stream velocities, being determined by the intersection of bottom and interfacial layers.

gard to Ekman dynamics, there is no significant cross-stream component to the stress. In a mixed planetary boundary layer this angle should deviate about 23° from opposition. Here, the mean angle is 1°, with a standard error of 5°. As mentioned above, the eddy viscosity in the bottom layer may be large enough such that the Ekman height is greater than the region of constant temperature, even greater than the bottom layer height. Thus, the velocity profile in the bottom layer does not develop the curvature expected in a planetary boundary layer. In most instances there is little curvature below the nose but a good deal within the strongly stratified interfacial layer (Fig. 4). A similar situation may sometimes occur at the base of the surface mixed layer (Gammelsrød 1975). Hence, the plume spreads as it flows downstream, with the dense bottom layer having a greater downslope velocity component than the lighter interfacial layer.

The bottom stresses oppose the plume direction, as expected. There is a correlation between the friction and nose velocities in both magnitude and direction. An average bottom stress is estimated for each section (open circles with error bars; Fig. 9). The individual bottom stress estimates within each section are weighted proportional to the distance between stations in the section averages. The mean ratio of the bottom stress and the square of the nose velocities (Fig. 7) is applied to the individual nose velocities to gain another estimate of the bottom stress at each point. This second estimate is used to construct error bars for each section average, using the same weighting scheme to calculate a standard error of the mean from the difference of the two stress estimates at each location. This error reflects the variability of the bottom stress estimates from friction velocities about the more steady but less direct estimates from the drag coefficient applied to the nose velocities. The bottom stress is high at section A, but peaks at about 2.5 Pa at section C, where the nose velocities are highest (Fig. 1). At section E the variability in stress estimates is larger, with the higher stress estimates coupled with comparatively low nose velocities, resulting in large error bars. By section F the stress is nearly an order of magnitude lower than at the other sections.

### *b. Turbulent buoyancy flux and interfacial stress estimates*

Here we estimate interfacial stress by dividing a bulk estimate of the sum of the turbulent kinetic energy dissipation and buoyancy flux by the mean shear in the interfacial layer. This sum is derived from bulk estimates of turbulent buoyancy flux. The turbulent buoyancy flux estimates are in turn derived from mean mass and volume transport budgets using the sections within the plume. The local turbulent energy balance consists of the transfer of energy from the mean flow by Reynolds stresses, the turbulent dissipation, and the turbulent buoyancy flux:

$$\rho\langle u'w'\rangle \frac{\partial U}{\partial z} = \epsilon + g\langle \rho' w'\rangle. \qquad (2)$$

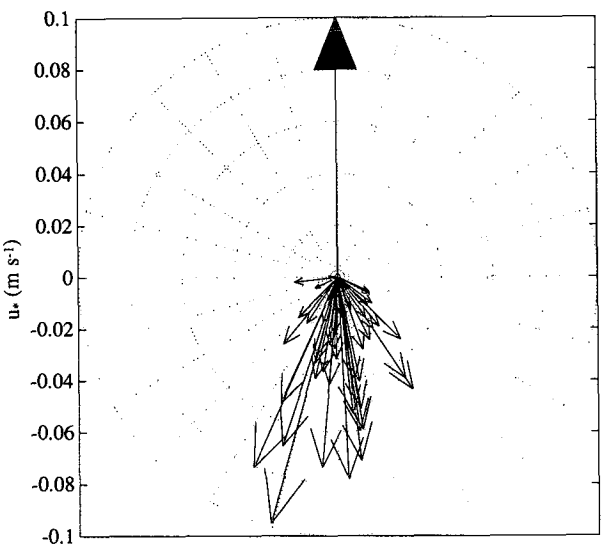


FIG. 8. Friction velocity magnitude and direction with respect to nose velocity direction (indicated by vector with filled head). Log-layer stress opposes the nose direction. In most profiles, curvature in the sense of a planetary boundary layer is found within the strongly stratified interfacial layer (Fig. 4).

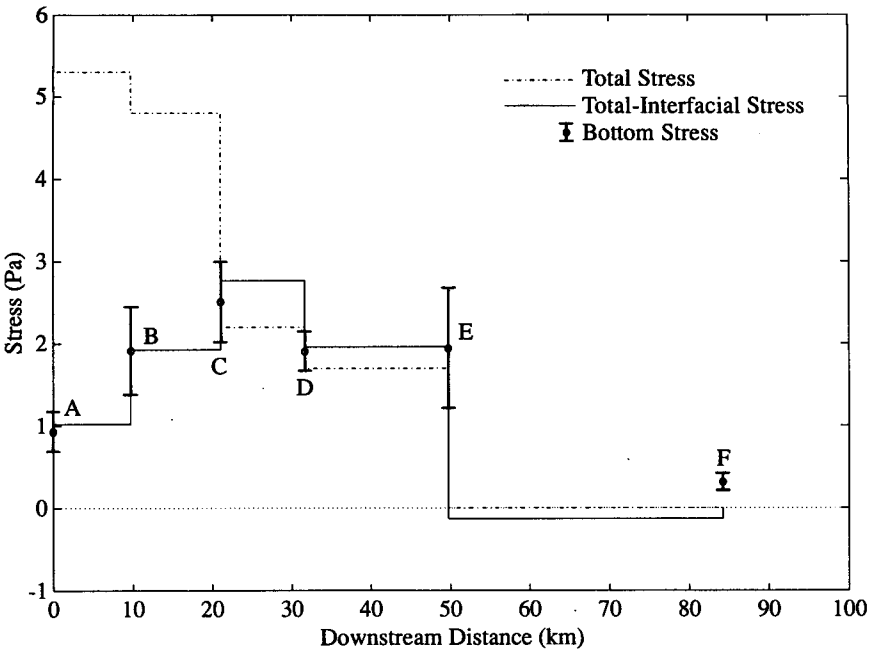


FIG. 9. Stresses on the Mediterranean outflow plume. Section-averaged bottom stresses from XCP velocity profiles (open circles with error bars for one standard error of the mean, or 68% confidence level of the mean) reach 2–3 Pa each by section C, decreasing an order of magnitude by section F. Bulk total stress estimates (dot–dashed line) are calculated from the residual of a bulk momentum budget (Baringer 1993). The differences of these and the bulk interfacial stress estimates give bulk values of bottom stress (solid line) that compare well with section averages of bottom stress from the velocity profiles (open circles).

Here the primed quantities are (in order of appearance) the fluctuations in horizontal velocity, vertical velocity, and density from their mean values. In most oceanic situations the turbulent buoyancy flux, $g\langle\rho' w'\rangle$, is thought to account for no more than 20% of this energy transfer, with over 80% going into turbulent dissipation $\epsilon$ (Osborn 1980).

The turbulent buoyancy flux can be estimated between station lines by taking advantage of conservation of mass and volume following Wesson (1991). Defining the top of the plume as where the mean velocity perpendicular to the section, $V$, crosses zero within the MW, and the horizontal cross section of the plume between the station lines as $S$, the mean velocity through the plume top, $W$, can be calculated between the station lines using volume conservation:

$$S_{ij}W_{ij} = \int_{A_i} V_i\,dA - \int_{A_j} V_j dA = T_i - T_j, \quad (3)$$

where the $A$ are the areas of the vertical cross sections of the plume at the station lines. The subscripts refer to two adjacent sections that bound the control volume on two sides. In the area of interest, the plume top meets the seafloor at each side of each section, enclosing the control volume on the other two sides. The top of the plume completes the control volume. Mass conservation over this control volume can be written as

$$S_{ij}(\rho_{ij}W_{ij} + \langle\rho' w'\rangle_{ij}) = \int_{A_i} \rho_i V_i\,dA - \int_{A_j} \rho_j V_j dA = M_i - M_j, \quad (4)$$

where the mass flux, $\rho W$, across the top of the control volume, $S$, has been separated into mean and turbulent components. We combine (3) and (4) to solve for the turbulent mass flux across the top of the volume:

$$\langle\rho' w'\rangle_{ij} = \frac{1}{S_{ij}}[M_i - M_j - \rho_{ij}(T_i - T_j)]. \quad (5)$$

The volume and mass transports are denoted by $T$ and $M$, respectively. Multiplying this quantity by the acceleration of gravity gives the turbulent buoyancy flux across the plume top between the two relevant sections. Presumably, this value is highest within the interfacial layer.

Bulk estimates of turbulent buoyancy flux are obtained using (5). Most of the dissipation of kinetic energy is through turbulent dissipation. The turbulent buoyancy flux is at most 0.2 of the dissipation, according to widely accepted estimates (Osborn 1980;

Itsweire et al. 1986). If this upper limit on mixing efficiency holds in the outflow plume, six times the turbulent buoyancy flux is a minimum estimate of the sum of the turbulent buoyancy flux and dissipation. The five bulk estimates made between each adjacent pair of the six sections can then be divided by the average of the mean shear in the interfacial layer, determined from the XCP data for each section pair, using (2) to obtain a lower bound on the stress in the interfacial layer between the sections. This stress is on the order of the bottom stress, being large between sections A and C, about 3–4 Pa, and small between the other sections. For comparison with the section-averaged bottom stresses (section 4a; open circles with error bars in Fig. 9) the bulk interfacial stresses are subtracted from the bulk total stresses (section 4c; dot–dashed line in Fig. 9) to give a residual bulk bottom stress (solid line in Fig. 9). As in the log layer, where velocity profile-based stresses exceed estimates from dissipation profiles, the bulk interfacial stresses are larger than local estimates based on dissipation measurements (JLS).

Calculating the turbulent buoyancy flux involves small differences of large numbers. The synoptic sections may have spatial or temporal sampling problems. Since the velocity and density fields are not independent, sampling problems in the mass flux at a particular section are likely to be proportional to those in the volume flux. These errors will partially cancel upon subtraction (5). Nonetheless, the estimates presented are crude; a 0.2 kg $m^{-3}$ error in the density at either section or a 0.2 Sv error in the volume transport could roughly double or zero the largest estimates between sections A and C. The mean and plume-top densities are relatively stable and probably accurate to 0.05 kg $m^{-3}$. The transport estimates, based on the conservation of MW, are accurate to 0.1 Sv. This error estimate for transports comes from the previously estimated uncertainty in the absolute velocity, about 0.05 m $s^{-1}$ normal to the sections. Applying these uncertainties to the calculation gives an uncertainty in the stress estimates of about 1 Pa. Thus small positive and negative values of interfacial stress between sections C and F are not significantly different from zero (Fig. 9). This error estimate assumes that the mean shear in the interfacial layer is well estimated, which it is, compared with these other quantities.

### c. *Total stress estimates from Bernoulli potential*

The total stress on the outflow can be estimated from an integrated form of the alongstream momentum equation. The flow is assumed to be semigeostrophic and quasi-parallel, confined to a broad thin layer on a gently sloping bottom. The equations of motion are integrated horizontally across the width of the outflow and vertically to the level where the downstream velocity crosses zero as described earlier. We define curvilinear coordinates where $\zeta$ is the alongstream coordinate and $\eta$ is the cross-stream coordinate. The alongstream momentum equation can then be written as

$$\frac{\partial}{\partial \zeta}\left(\int_A \rho u^2 dA\right) = -\int_A \frac{\partial p}{\partial \zeta} dA - \int_{-l}^{+l} (\tau_B - \tau_I) d\eta, \tag{6}$$

where the horizontal limits of the flow are $\eta = \pm l$ and $\tau_B$ is the bottom stress. The stress at the depth where the alongstream velocity is zero is $\tau_I$, the interfacial stress. If the fluid above the outflow were motionless, $\tau_I$ would vanish and the total stress would be equivalent to the bottom stress. Since there is flow above the outflow near the Strait of Gibraltar, the interfacial stress $\tau_I$ does not vanish there, being proportional to $\partial u/\partial z$.

The balance used is similar to that of Smith (1975) except that no thin jet approximation has been used to simplify the pressure gradient term in (6). This equation can be rewritten as a Bernoulli function where downstream changes in pressure (or potential energy) and kinetic energy are balanced by the total stress (Baringer 1993). The total stress is evaluated in this manner using the XCP and CTD data (Fig. 9). Total stress is greater than 5 Pa between sections A and C, decreasing to about 1 Pa downstream.

The greatest uncertainty in this calculation arises from the evaluation of the downstream derivative. Downstream distances, and hence $\partial/\partial\zeta$, are calculated using the center of the density anomaly of each section. The average downstream position of each section could also be defined as the geographic center, the center of mass, or the center of mass flux. Because the section spacing is close, these different positions can change the total stress estimate by as much as 20%. Therefore, the uncertainty is about 1 Pa east of section C and about 0.5 Pa west of section C.

## 5. Conclusions

The analysis presented here reveals the two-layer vertical structure of the Mediterranean outflow plume and the importance of bottom and interfacial stresses in maintaining that structure. Most of the Ekman veering occurs in the highly sheared, highly stratified interfacial layer, where the MW fraction and downstream velocity increase rapidly. The nearly linear $T$–$S$ structure within the plume suggests strong mixing there. At the plume nose, the downstream velocity is at a maximum, which isolates the interfacial layer from the bottom layer. In the bottom layer, the MW fraction is more nearly homogeneous, with only a small increase from the nose to the bottom; however, downstream velocity decreases rapidly toward the bottom. This high shear in the presence of small stratification suggests vigorous mixing within this layer.

One goal of the experiment was to quantify the stresses on the plume. The "profile method" for determining the bottom stress from XCP velocity data appears to work well. The stress estimated from the log-layer fit has a direction that opposes the plume's mean flow direction. There is a slight veering of the stress in the sense predicted by Ekman dynamics. In another approach, the XCP and CTD data have been used to construct a downstream momentum budget for the six sections across the plume (Baringer 1993). The rate of change in Bernoulli potential with downstream distance gives an indirect estimate of the stress on the plume.

The estimates of the stress from the log-layer fits are used to obtain an independent estimate of the mean bottom stress at each of the six sections (section 4a). The temporal variability of the bottom stress at sites of multiple XCP drops is small. Nevertheless, as the velocity of the plume varies across each section, so do the individual estimates of bottom stress across each section. Thus, the means of the bottom stresses calculated for each section are weighted by distance between stations (Fig. 9). Bulk estimates of total stress on the plume are made from momentum budget residuals (section 4c; Baringer 1993). The bulk values of interfacial stresses (section 4b) are subtracted from these total stress estimates. The result is a set of bulk bottom stress values that agree with the section-averaged bottom stresses to within the error bars (Fig. 9). Both sets of bottom stresses increase from 1 to 2.5 Pa from section A to C, while the total stress between these sections is around 5 Pa, owing to high interfacial stresses in this region of strong entrainment. From section C to section F, the bulk and section-average bottom stresses fall from near 2 to below 1 Pa, as does the total stress. The biggest plume stresses are an order of magnitude larger than mean wind stress values over the ocean gyres. As the plume flows down the slope its acceleration is limited by these strong bottom and interfacial stresses.

Dissipation measurements taken during the experiment yield bottom stress estimates with a similar pattern but a magnitude that is smaller by about a factor of three (JLS). Estimates of the ratio of interfacial layer to bottom layer stress suggest that the interfacial stress is of the same magnitude as the bottom stress where the total stress is largest. Thus estimates of interfacial stress from dissipation and shear measurements (JLS) are also smaller than the bulk estimates presented here.

*Acknowledgments.* This work was supported by the United States Office of Naval Research. The data were collected under Contract N00014-87-K-004, and subsequent analysis was completed under Grant N00014-90-J-1100, both to the Applied Physics Laboratory of the University of Washington. GCJ received additional support from the National Oceanic and Atmospheric Administration's Office of Global Programs. We are indebted to the ship's company and scientific parties on board leg V of R/V *Oceanus* cruise 202 for their assistance in gathering the data. Special thanks to Gregorio Parrilla for his assistance with the CTD observations, and Alain Cantos for his assistance with the XCP processing. Eric Kunze developed the XCP acquisition software. John Dunlap and Robert Drever provided engineering support for the field work. Maureen Kennelly did much of the data processing. M. Dickson Allison assisted with the data analysis. PMEL Contribution Number 1498.

## REFERENCES

Ambar, I., and M. R. Howe, 1979: Observations of the Mediterranean outflow—I. Mixing in the Mediterranean outflow. *Deep-Sea Res.*, **26,** 535–554.

Armi, L., and D. M. Farmer, 1988: The flow of Mediterranean water through the Strait of Gibraltar. *Progress in Oceanography,* Vol. 21, Pergamon Press, 1–105.

——, D. Hebert, N. Oakey, J. Price, P. L. Richardson, T. Rossby, and B. Ruddick, 1989: Two years in the life of a Mediterranean salt lens. *J. Phys. Oceanogr.*, **19,** 354–370.

Baringer, M. O., 1993: Mixing and dynamics of the Mediterranean outflow. Ph.D. thesis, MIT/WHOI, WHOI-93-52, 244 pp.

——, and J. F. Price, 1990: A simple model of the descending Mediterranean outflow plume. *The Physical Oceanography of Sea Straits,* L. J. Pratt, Ed., Kluwer Academic, 537–544.

Bormans, M., and J. S. Turner, 1990: The formation of the doubly stable stratification in the Mediterranean outflow. *Deep-Sea Res.*, **37,** 1697–1712.

Bryden, H. L., and T. H. Kinder, 1991: Steady two-layer exchange through the Strait of Gibraltar. *Deep-Sea Res.*, **38**(Suppl. 1), S445–S463.

——, E. C. Brady, and R. D. Pillsbury, 1989: Flow through the Strait of Gibraltar. *Seminario Sobre La Oceanografia Fisica Del Estrecho De Gibraltar,* Madrid, SECEG, 166–194.

Candela, J. C., C. D. Winant, and H. L. Bryden, 1989: Meteorologically forced subinertial flows through the Strait of Gibraltar. *J. Geophys. Res.*, **94,** 12 667–12 679.

Gammelsrød, T., 1975: Instability of Couette flow in a rotating fluid and origin of Langmuir circulations. *J. Geophys. Res.*, **80,** 5069–5075.

Hebert, D., N. Oakey, and B. Ruddick, 1990: Evolution of a Mediterranean salt lens: Scalar properties. *J. Phys. Oceanogr.*, **20,** 1468–1483.

Heezen, B. C., and G. L. Johnson, 1969: Mediterranean undercurrent and microphysiography west of Gibraltar. *Bull. Inst. Oceanogr. Monaco,* **67,** 1–51.

Holton, J. R., 1979: *An Introduction to Dynamic Meteorology.* Academic Press, 391 pp.

Itsweire, E. C., K. N. Helland, and C. W. Van Atta, 1986: The evolution of grid-generated turbulence in a stably stratified fluid. *J. Fluid Mech.*, **163,** 299–338.

Johnson, G. C., and T. B. Sanford, 1992: Secondary circulation in the Faroe Bank channel outflow. *J. Phys. Oceanogr.*, **22,** 927–933.

——, R. G. Lueck, and T. B. Sanford, 1994: Stress on the Mediterranean outflow plume: Part II. Dissipation and shear measurements. *J. Phys. Oceanogr.*, **24,** 2084–2092.

Jones, D. W., 1989: Velocity profiler (XCP) observations of a bottom boundary layer in the Strait of Juan de Fuca. APL-UW TR 8927, Applied Physics Laboratory, University of Washington, Seattle, WA, 209 pp.

Kennelly, M. A., J. H. Dunlap, T. B. Sanford, E. L. Kunze, M. D. Prater, and R. G. Drever, 1989a: The Gulf of Cadiz expedition:

R/V *Oceanus* cruise 202. APL-UW TR 8914, Applied Physics Laboratory, University of Washington, Seattle, WA, 115 pp.

——, T. B. Sanford, and T. W. Lehman, 1989b: CTD data from the Gulf of Cadiz expedition: R/V *Oceanus* cruise 202. APL-UW TR 8917, Applied Physics Laboratory, University of Washington, Seattle, WA, 129 pp.

——, M. D. Prater, J. H. Dunlap, E. L. Kunze, and T. B. Sanford, 1989c: XCP data from the Gulf of Cadiz expedition: R/V *Oceanus* cruise 202. APL-UW TR 8925, Applied Physics Laboratory, University of Washington, Seattle, WA, 206 pp.

Killworth, P. D., 1983: On the motion of isolated lenses on a beta-plane. *J. Phys. Oceanogr.*, **13,** 368–376.

McDougall, T. J., 1990: Bulk properties of "hot smoker" plumes. *Earth Planet. Sci. Lett.*, **99,** 185–194.

McDowell, S. E., and H. T. Rossby, 1978: Mediterranean water: An intense mesoscale eddy off the Bahamas. *Science,* **202,** 1085–1087.

Ochoa, J., and N. A. Bray, 1991: Water mass exchange in the Gulf of Cadiz. *Deep-Sea Res.*, **38**(Suppl. 1), S465–S503.

Osborn, T. R., 1980: Estimates of the local rate of vertical diffusion from dissipation estimates. *J. Phys. Oceanogr.*, **10,** 83–89.

Prater, M. D., 1991: A method for depth and temperature correction of expendable probes. *J. Atmos. Oceanic Technol.*, **8,** 888–894.

Price, J. F., M. O. Baringer, R. G. Lueck, G. C. Johnson, I. Ambar, G. Parrilla, A. Cantos, M. A. Kennelly, and T. B. Sanford, 1993: Mediterranean outflow mixing and dynamics. *Science,* **259,** 1277–1282.

Reid, J. L., 1979: On the contribution of the Mediterranean Sea outflow to the Norwegian–Greenland Sea. *Deep-Sea Res.*, **26,** 1199–1223.

Sanford, T. B., R. G. Drever, J. H. Dunlap, and E. A. D'Asaro, 1982: Design, operation and performance of an expendable temperature and velocity profiler (XTVP). APL-UW TR 8110, Applied Physics Laboratory, University of Washington, 83 pp.

Smith, P. C., 1975: A streamtube model for bottom boundary currents in the ocean. *Deep-Sea Res.*, **22,** 853–873.

Wesson, J. C., 1991: Turbulence and mixing in the Strait of Gibraltar. Ph.D. thesis, University of Washington, 316 pp.

Worthington, L. V., 1976: On the North Atlantic circulation. *The Johns Hopkins Oceanographic Studies,* No. 6, 110 pp.